

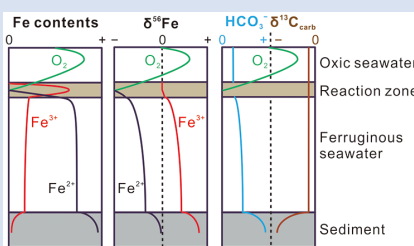
Isotope evidence for the coupled iron and carbon cycles 1.4 billion years ago

H.J. Wang¹, Y.T. Ye^{1,2}, Y. Deng^{1,2}, X.M. Wang¹, E.U. Hammarlund^{3,4},
H.F. Fan⁵, D.E. Canfield^{1,3*}, S.C. Zhang^{1*}



<https://doi.org/10.7185/geochemlet.2208>

Abstract



Although ferruginous waters were widespread in the deep ocean until 0.58 Ga, massive Fe deposits were rare during the interval from 1.8–0.8 Ga. Here, we report the contents and isotopic compositions of Fe and C from the ~1.4 Ga Xiamaling (XML) siderite deposits, North China. A genetic model is introduced to interpret the dynamic and coupled Fe and C cycles in Mesoproterozoic oceans and sediments. Although the positive Eu anomalies of XML siderites are relatively low in the XML deposits, an enhanced input of hydrothermal Fe²⁺ is recognised from the isotopic compositions of Fe and C. Hydrothermal fluid is suggested as a key controlling factor during the XML siderite deposition.

Received 6 October 2021 | Accepted 16 February 2022 | Published 14 March 2022

Introduction

Most marine massive Fe deposits formed 3.0–1.8 Ga, with a billion-year hiatus until a brief return around 0.8 Ga (Konhauser *et al.*, 2017). During this gap period, the iron formation (IF) shortage was thought to be a result of significantly decreased Fe²⁺ concentrations in the ocean, which was either substantially oxidised (Holland, 1990) or sulfurised (Canfield, 1998). Recent studies provide increasing evidence that ferruginous water was still widespread in the deep ocean until 0.58 Ga (Canfield *et al.*, 2008). Although atmospheric oxygen levels are still controversial in the time window of 1.8–0.8 Ga (Planavsky *et al.*, 2014; Zhang *et al.*, 2016, 2021; Canfield *et al.*, 2021), it is believed that oxygen was deficient compared to the last 0.7 Ga.

Thus, although IF deposition is limited from 1.8–0.8 Ga, there are recent reports of significant ferrous carbonate deposition generating siderite-dominated IFs, such as the ~1.40 Ga Xiamaling (XML) IF in North China (Canfield *et al.*, 2018; Tang *et al.*, 2018) and the ~1.33 Ga Jingtieshan IF in Qilian (Yang *et al.*, 2018). Siderite deposits are also found in the ~1.45 Ga Sherwin ironstone in Australia (Planavsky *et al.*, 2014). To further explore the mechanisms of siderite-dominated IF deposition and the associated marine Fe and C cycles, we analysed the contents and isotopic compositions of Fe and C of the XML IF. Combined with the reported data in Canfield *et al.* (2018), our results show evidence for hydrothermal Fe²⁺ input during the deposition of XML IF, where the Fe and C cycles were tightly coupled.

Geological Background and Samples

Samples were obtained from a core in the Xihuayuan region located in the Yanliao Basin, which was an offshore basin in North China during the breakup of the Columbia supercontinent (Fig. 1a–c). The XML IF is found over 45 m of stratigraphic thickness and is defined as unit 5, which can be further divided into the lower part with greyish-black mudstone and the upper part with green sandy mudstone (Fig. 1d). Centimetre- to decimetre-sized laminar and nodular siderites are embedded in the clastic rocks (Fig. 1e–h), indicating a pore-water diagenetic environment. Detailed information of the geological background is in the Supplementary Information (SI).

Methods and Results

As the normal Fe extraction protocol in Poulton and Canfield (2005) proved ineffective at removing siderite from our IF samples, an acid extraction method was used. We used ferrozine to determine the contents of acid-soluble Fe²⁺, and used ferrozine with the addition of hydroxylamine to determine the sum of Fe²⁺ and Fe³⁺. On separate samples, the Cr-reduction method was used to quantify the Fe bound in pyrite (Fe_{py}). Iron isotope values (δ⁵⁶Fe) from whole rock samples were determined and expressed as the ⁵⁶Fe/⁵⁴Fe ratio relative to IRMM-014. Contents of total organic carbon (TOC), elements and main diagenetic minerals of whole rock samples were also determined. The isotopic composition of carbonate (δ¹³C_{carb}) of the IF samples and the isotopic composition of organic carbon (δ¹³C_{org}) of the clastic samples

1. Research Institute of Petroleum Exploration and Development, Beijing 100083, China
 2. School of Earth and Space Sciences, Peking University, Beijing 100871, China
 3. Nordcee and Institute of Biology, University of Southern Denmark, Odense 5230, Denmark
 4. Department of Geology, Lund University, Lund 22362, Sweden
 5. Institute of Geochemistry, Chinese Academy of Sciences, Guiyang 550002, China
- * Corresponding author (email: sczhang@petrochina.com.cn, dec@biology.sdu.dk)



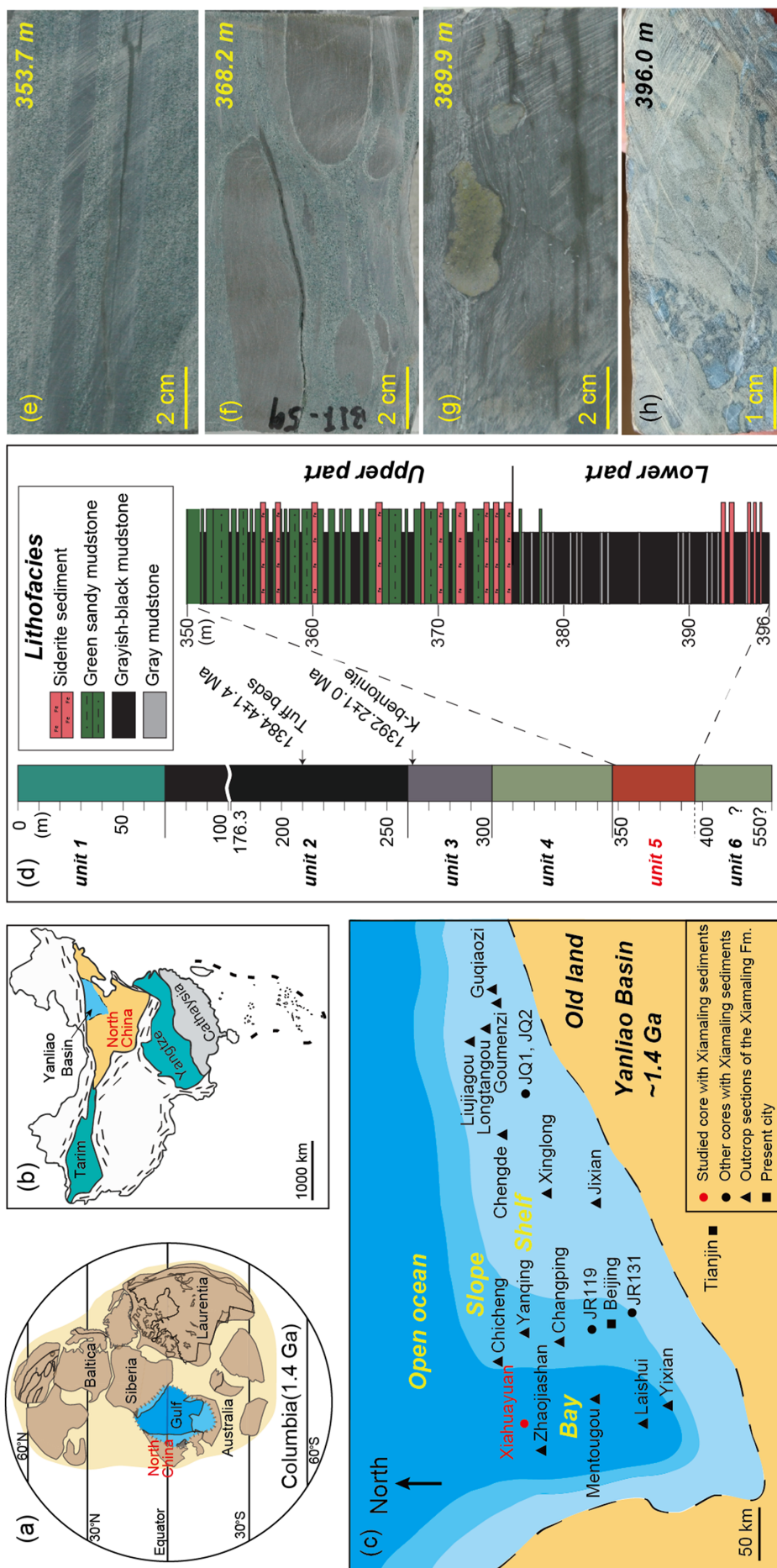


Figure 1 Location of the (a) 1.4 Ga and (b) present North China Craton, modified from Zhang et al. (2021). (c) Paleogeography of the Yanliao Basin 1.4 Ga, modified from Lyu et al. (2021). (d) Stratigraphy of iron formation defined as unit 5 of the Xiamaling Formation. Photos of laminar (e) and nodular (f–h) siderites from the core in the Xiahuyuan region.

were determined and expressed relative to VPDB. Detailed methods are in the SI.

Geochemical data of the IF samples (defined as samples with total Fe (Fe_T) > 15 %) and the interbedded clastic rocks are illustrated in Figure 2 and Table S-1. As has been observed in the upper part (discussed in Canfield *et al.*, 2018), siderite is the dominant diagenetic mineral of the lower IF samples (Table S-1). The lower IF samples have extremely high Fe_T/Al ratios (mostly >15) and Fe_T/Ti ratios (mostly >200), high Fe^{2+}/Fe_T ratios (>0.8), extremely low Fe^{3+}/Fe_T ratios (<0.02) and Fe_{py}/Fe_T ratios (<0.01), and negative $\delta^{56}Fe$ values (from -0.53 ‰ to -0.34 ‰). In contrast, the interbedded clastic rocks of the lower IF have low Fe_T/Al ratios (~0.46) and Fe_T/Ti ratios (mostly from 4 to 10), medium Fe^{2+}/Fe_T ratios (from 0.17 to 0.74), low Fe^{3+}/Fe_T ratios (<0.1), medium Fe_{py}/Fe_T ratios (from 0.01 to 0.3), and positive $\delta^{56}Fe$ values (mostly

from +0.19 ‰ to +0.72 ‰). The upper IF samples also have high Fe_T/Al ratios (mostly from 3 to 15) and Fe_T/Ti ratios (mostly from 30 to 200), high Fe^{2+}/Fe_T ratios (>0.8), low Fe^{3+}/Fe_T ratios (<0.15), extremely low Fe_{py}/Fe_T ratios (<0.01), and more negative $\delta^{56}Fe$ values (from -1.20 ‰ to -0.32 ‰) than those of the lower IF samples. The interbedded clastic rocks of the upper IF have medium Fe_T/Al ratios (from 0.5 to 2.7) and Fe_T/Ti ratios (mostly from 10 to 30), medium Fe^{2+}/Fe_T ratios (from 0.46 to 0.83), low Fe^{3+}/Fe_T ratios (<0.15), extremely low Fe_{py}/Fe_T ratios (<0.01), and fluctuating $\delta^{56}Fe$ values (from -0.71 ‰ to +0.38 ‰). The sedimentary rocks of the lower part (including the IF samples) have higher TOC values (mostly from 0.3 % to 1.0 %) than those of the upper part (mostly <0.3 %). The $\delta^{13}C_{org}$ values of most samples were between -33 ‰ and -32 ‰, while the $\delta^{13}C_{carb}$ values of the IF samples fluctuated from -27 ‰ to -8 ‰.

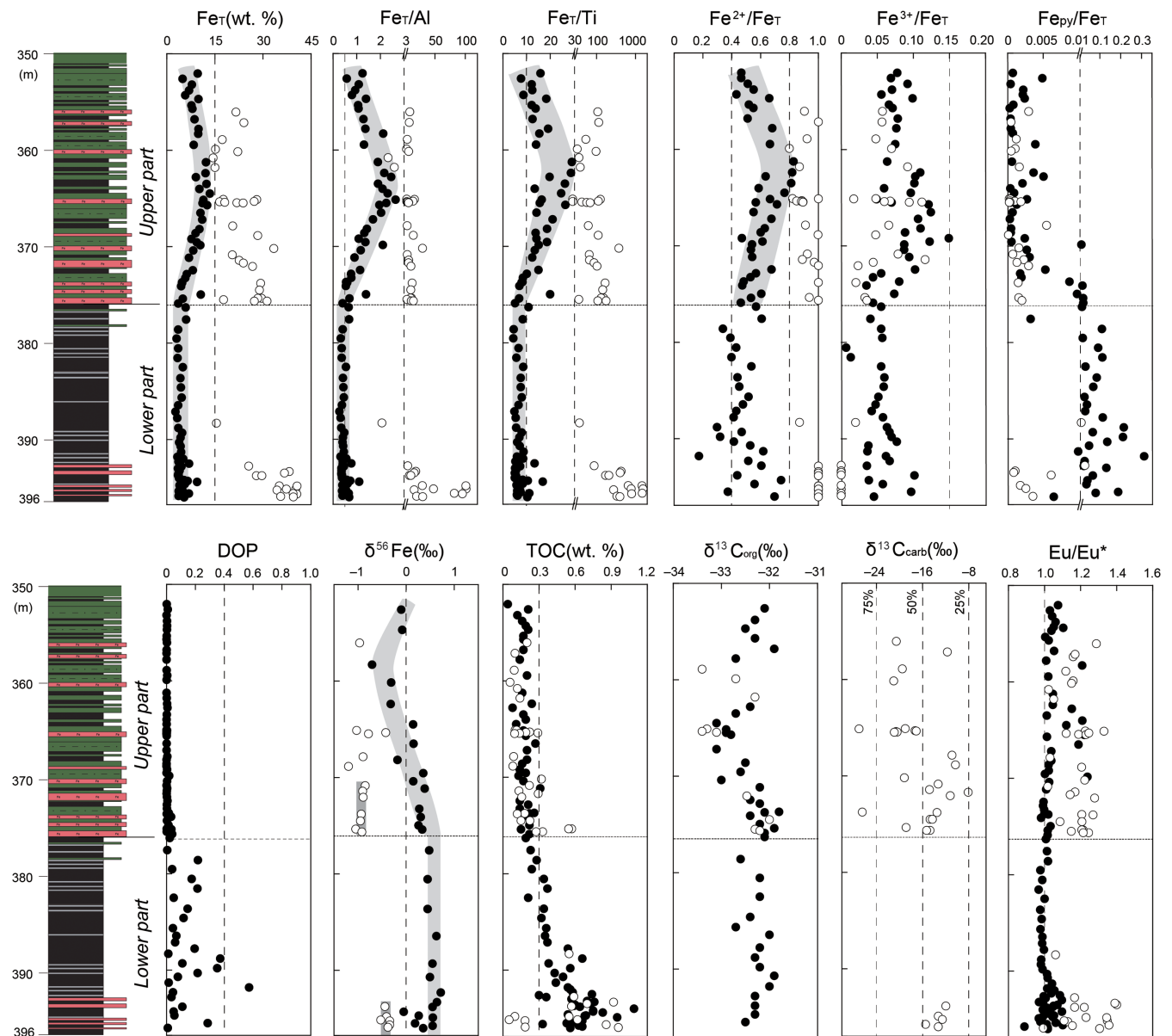


Figure 2 Geochemical profiles of the unit 5 of the Xiamaling Formation. Degree of pyritisation (DOP) was calculated by $Fe_{py}/(Fe^{2+}+Fe^{3+}+Fe_{py})$. Data of the Fe_T , total organic carbon (TOC), Eu/Eu^* , carbon isotopes of carbonate ($\delta^{13}C_{carb}$) and kerogen ($\delta^{13}C_{org}$) with a depth range of 390–350 m were from Canfield *et al.* (2018). Note the abscissa breaks of Fe_T/Al , Fe_T/Ti , Fe_{py}/Fe_T are at 3, 30 and 0.01, respectively. Cycle and solid points represent IF ($Fe_T > 15\%$) and clastic ($Fe_T < 15\%$) samples, respectively. Dashed lines in the $\delta^{13}C_{carb}$ panel represent the proportions of organic-sourced bicarbonate of measured samples, with an initial $\delta^{13}C_{org}$ of -32 ‰ and an initial $\delta^{13}C$ of bicarbonate in water column of 0 ‰.

Depositional Redox Environments

We could not use standard Fe speciation protocols on the siderite-rich samples, but high Fe_T/Al ratios (Lyons and Severmann, 2006) and high Fe_T/Ti ratios (Dauphas *et al.*, 2004), combined with high $\text{Fe}^{2+}/\text{Fe}_T$ ratios (>0.8) and extremely low $\text{Fe}_{\text{py}}/\text{Fe}_T$ ratios (<0.01) confirmed ferruginous conditions during the IF deposition, consistent with the previous redox-sensitive element proxies from Canfield *et al.* (2018) and Tang *et al.* (2018). As we did not use the standard Fe speciation protocol, water column redox conditions in the clastic rocks could only be evaluated where the Fe_T/Al and Fe_T/Ti ratios well exceeded the crustal average values (~ 0.5 and ~ 10 , respectively, Rudnick and Gao, 2003). For the clastic rocks of the upper part, high Fe_T/Al ratios (0.5–2.7), high Fe_T/Ti ratios (10–30) and extremely low sulfurised Fe ratios ($\text{Fe}_{\text{py}}/\text{Fe}_T < 0.01$) indicate ferruginous deposition conditions. For clastic rocks of the lower part, the Fe_T/Al and Fe_T/Ti ratios hover around the crustal average values, and the sulfurised Fe ratios range from 0.01 to 0.3, so the redox conditions during deposition are still uncertain. However, a euxinic depositional environment can be excluded, as it needs a degree of iron pyritisation (DOP) of at least 0.4 (Raiswell and Canfield, 2012).

Sources of the Iron

Positive Eu anomalies (Eu/Eu^* ratios 1.0–1.4) for all IF samples (Fig. 2) indicate a hydrothermal impact on the water chemistry during the IF formation, and hydrothermal Fe^{2+} may have been the most important source of Fe^{2+} to the Precambrian ocean (Johnson *et al.*, 2020). During the deposition of the XML IF, a hydrothermal Fe^{2+} source may be associated with the breakup of the supercontinent Columbia (Tang *et al.*, 2018). However, the positive Eu anomalies of the XML IF are rather muted when compared with the ~ 1.3 Ga Jingtieshan IF (Eu/Eu^* ratios 4.4–6.5) (Yang *et al.*, 2018), so the XML IF may be rather distal from the hydrothermal source.

Another source of Fe^{2+} to seawater is released from clastic particulates depositing in anoxic waters on the shelf (Raiswell and Canfield, 2012). Indeed, a benthic clastic source of dissolved Fe^{2+} likely supplies most Fe that accumulates as reactive Fe in

anoxic depositional environments today, as revealed through sequential sediment extractions (Raiswell and Canfield, 2012).

Iron Isotope Fractionation Models

Formation of the XML IF has been suggested to result from three steps (Canfield *et al.*, 2018), including: 1) oxidation of seawater Fe^{2+} to Fe-oxyhydroxides ($\text{Fe}(\text{OH})_3$), likely at the chemocline of the ancient marine basin, 2) reduction of $\text{Fe}(\text{OH})_3$ to diagenetic Fe^{2+} in the water column and sediments, and 3) crystallisation of Fe^{2+} as siderite. Whole rock $\delta^{56}\text{Fe}$ values would be affected by the initial $\delta^{56}\text{Fe}$ of seawater Fe^{2+} and the net isotopic fractionation between products and reactants ($\Delta^{56}\text{Fe}_{\text{product-reactant}}$) in the above steps. These steps are presented in Figure 3 and are reviewed in more detail in Johnson *et al.* (2020) as well as the SI.

To briefly summarise, the oxidation of Fe^{2+} generates ^{56}Fe -enriched $\text{Fe}(\text{OH})_3$ (Fe^{3+}) compared to the Fe^{2+} source. With the subsequent reduction of this Fe^{3+} , and generation of diagenetic Fe^{2+} , both the Fe^{2+} product and the residual Fe^{3+} will be progressively ^{56}Fe -enriched. Due to the $\Delta^{56}\text{Fe}_{\text{Fe(II)-Fe(III)}}$ of diagenetic Fe^{2+} and residual Fe^{3+} , whole rock $\delta^{56}\text{Fe}$ values in clastic rocks with residual Fe^{3+} are generally heavier than the Fe^{2+} in siderite alone. For the higher molar ratio of Fe^{2+} and bicarbonate (HCO_3^-) as products during step 2 (4:1) than as reactants in step 3 (1:1), excessive diagenetic Fe^{2+} diffuse upwards and/or insufficient HCO_3^- diffuse downwards during step 3. Because of the different isotopic trends of diagenetic Fe^{2+} and HCO_3^- , the $\delta^{56}\text{Fe}$ and $\delta^{13}\text{C}_{\text{carb}}$ of siderite depend on the position of its precipitation. The genetic model shown in Figure 3 is illustrative only, not quantitative, but the trends in $\delta^{56}\text{Fe}$ are similar to those reproduced in the open system diffusion/reaction model (Johnson *et al.*, 2020).

Dynamic Iron Cycle in the 1.4 Ga Marine Environment

The $\delta^{56}\text{Fe}$ values of both lower and upper IF samples are significantly reduced compared to those of the clastic rocks in the same intervals (Fig. 2). With an average Fe content in the upper crust of

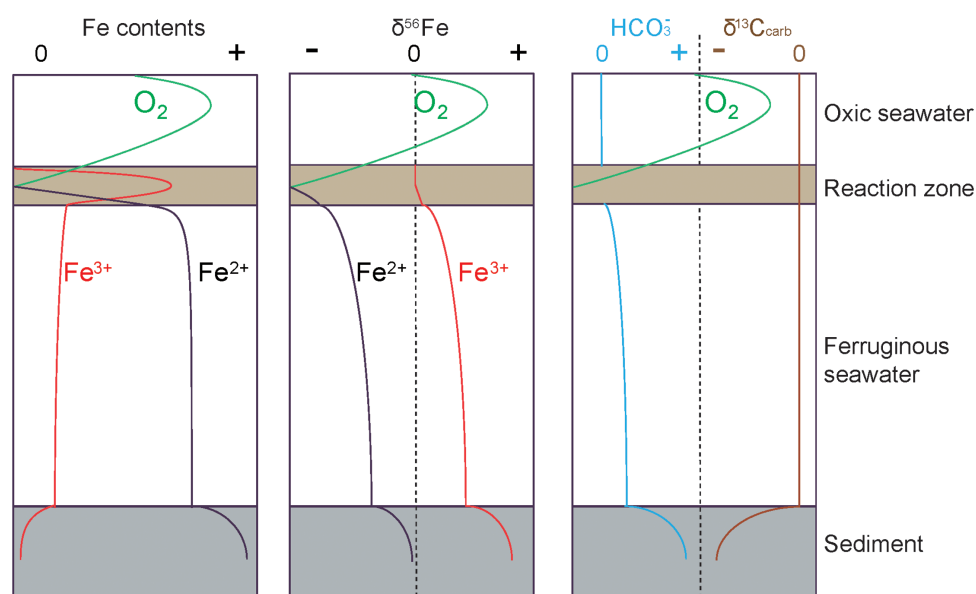


Figure 3 Genetic model of the coupled Fe and C cycles and isotope fractionations in the water column and sediment.

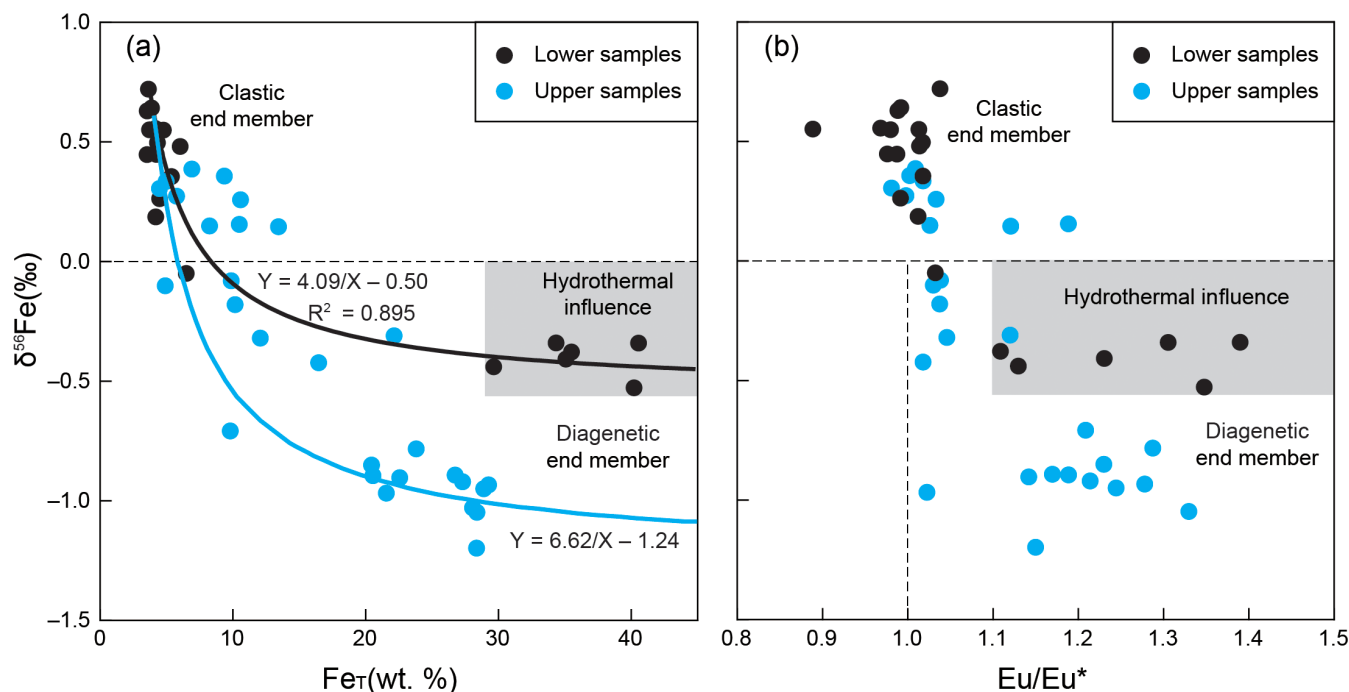


Figure 4 Correlation diagrams of $\delta^{56}\text{Fe}$ with (a) Fe_t and (b) Eu/Eu^* . The black and blue lines in (a) are the optimal mixing lines of the lower and upper parts, respectively, with a clastic end member and a diagenetic end member. Grey areas mean the Fe cycle and $\delta^{56}\text{Fe}$ values were influenced by the hydrothermal fluids.

3.6 % (Rudnick and Gao, 2003), and for siderite of 48 %, rocks in the lower part are consistent with the mixing of a clastic end-member with a $\delta^{56}\text{Fe}$ value of +0.6 ‰ and a diagenetic siderite end member with a $\delta^{56}\text{Fe}$ value of -0.4 ‰ ($R^2 = 0.895$, Fig. 4a), which is close to the measured $\delta^{56}\text{Fe}$ values (from -0.53 ‰ to -0.34 ‰) of IF samples. However, for the upper part, the optimal $\delta^{56}\text{Fe}$ value of the diagenetic siderite was -1.1 ‰, with a $\delta^{56}\text{Fe}$ value of the clastic end member also set to +0.6 ‰ (Fig. 4a). Thus, the circumstances of IF formation in the lower and upper parts were clearly different. Details of the calculation method are in the SI.

Moreover, the $\delta^{13}\text{C}_{\text{carb}}$ values of IF samples are much more ^{13}C -depleted than the Mesoproterozoic seawater HCO_3^- (~0 ‰, Saltzman and Thomas, 2012), supporting the idea that the siderites most likely precipitated in diagenetic sediment environments with varied and limited exchange with the overlying waters. The $\delta^{13}\text{C}_{\text{carb}}$ values of siderites from the lower part are from -15 ‰ to -12 ‰, and thus more ^{13}C -enriched than most samples from the upper part (Fig. 2). This difference in $\delta^{13}\text{C}_{\text{carb}}$ values would suggest that the siderite from the lower part precipitated closer to the water-sediment interface, with a greater seawater HCO_3^- contribution, when compared to the siderites from the upper part (Fig. 3). Following this logic, if we assume that the patterns of water column $\delta^{56}\text{Fe}$ values remained similar during all of the XML IF formation, the siderites from the lower part should be more ^{56}Fe -depleted than those from the upper part (Fig. 3). However, the elevated $\delta^{56}\text{Fe}$ values (from -1.1 ‰ to -0.4 ‰) contradict this hypothesis and indicate more ^{56}Fe -enriched water in the Yanliao Basin during the IF formation in the lower part.

We propose that the lower part of the XML IF received an enhanced input of hydrothermal fluids with $\delta^{56}\text{Fe}$ values of 0 ‰. The hydrothermal fluids with elevated Fe^{2+} concentrations (German *et al.*, 1990) generated higher Fe^{2+} concentrations and elevated $\delta^{56}\text{Fe}$ values in the bottom waters of the Yanliao Basin. Higher Fe^{2+} concentrations would have resulted in

siderite precipitation with lower HCO_3^- concentrations and closer to the sediment-water interface, consistent with heavier $\delta^{13}\text{C}_{\text{carb}}$ values of siderites from the lower part. Higher Fe^{2+} concentrations could have also elevated the rates of Fe-associated primary production, leading to higher values of TOC (Fig. 2).

Generally, the positive Eu anomalies of the XML IF can be taken to indicate hydrothermal contributions. We also note that the positive Eu anomalies are relatively small and of the same magnitude in both the upper and lower IFs. Overall, the positive Eu anomalies in the IFs (Fig. 4b) do support a hydrothermal source of Fe^{2+} to the Yanliao Basin. This conclusion is consistent with the enhanced hydrothermal Fe^{2+} supply that we argue impacted both the $\delta^{56}\text{Fe}$ and $\delta^{13}\text{C}_{\text{carb}}$ values of the lower XML IF.

Implications on Marine Iron and Carbon Cycles

The XML IF was formed within a ferruginous marine basin with an active iron cycle that was intimately coupled to the C cycle. However, there are differences in the dynamics of the Fe and C cycles in the upper and lower parts of the sedimentary sequence where the IFs are formed. In particular, an enhanced hydrothermal Fe^{2+} contribution elevated the concentrations of Fe^{2+} in the water column and the rates of Fe associated with the C cycle in the lower IF, and should be a key controlling factor in regulating the rates of Fe associated with marine primary production during the siderite-dominated XML IF formation.

Acknowledgements

We thank Zhihong Li, Heidi Jensen and Iben Rosendahl for the experimental analysis. The research is financially supported by the Strategic Priority Research Program of the Chinese Academy of Sciences (XDA14010101), National Key Research



and Development Program of China (2017YFC0603101), National Natural Science Foundation of China (41872125, 42102146) and Villum Foundation (16518).

Editor: Claudine Stirling

Additional Information

Supplementary Information accompanies this letter at <https://www.geochemicalperspectivesletters.org/article2208>.



© 2022 The Authors. This work is distributed under the Creative Commons Attribution Non-Commercial No-Derivatives 4.0

License, which permits unrestricted distribution provided the original author and source are credited. The material may not be adapted (remixed, transformed or built upon) or used for commercial purposes without written permission from the author. Additional information is available at <https://www.geochemicalperspectivesletters.org/copyright-and-permissions>.

Cite this letter as: Wang, H.J., Ye, Y.T., Deng, Y., Wang, X.M., Hammarlund, E.U., Fan, H.F., Canfield, D.E., Zhang, S.C. (2022) Isotope evidence for the coupled iron and carbon cycles 1.4 billion years ago. *Geochem. Persp. Let.* 21, 1–6. <https://doi.org/10.7185/geochemlet.2208>

References

- CANFIELD, D.E. (1998) A new model for Proterozoic ocean chemistry. *Nature* 396, 450–453. <https://doi.org/10.1038/24839>
- CANFIELD, D.E., POULTON, S.W., KNOLL, A.H., NARBONNE, G.M., ROSS, G., GOLDBERG, T., STRAUSS, H. (2008) Ferruginous conditions dominated later neoproterozoic deep-water chemistry. *Science* 321, 949–952. <https://doi.org/10.1126/science.1154499>
- CANFIELD, D.E., ZHANG, S.C., WANG, H.J., WANG, X.M., ZHAO, W.Z., SU, J., BJERRUM, C.J., HAXEN, E.R., HAMMARLUND, E.U. (2018) A Mesoproterozoic Iron Formation. *Proceedings of the National Academy of Sciences* 115, E3895–E3904. <https://doi.org/10.1073/pnas.1720529115>
- CANFIELD, D.E., VAN ZUILEN, M.A., NABHAN, S., BJERRUM, C.J., ZHANG, S.C., WANG, H.J., WANG, X.M. (2021) Petrographic carbon in ancient sediments constrains Proterozoic Era atmospheric oxygen levels. *Proceedings of the National Academy of Sciences* 118, e2101544118. <https://doi.org/10.1073/pnas.2101544118>
- DAUPHAS, N., VAN ZUILEN, M., WADHWA, M., DAVIS, A.M., MARTY, B.J., PHILIP, E. (2004) Clues from Fe isotope variations on the origin of early Archean BIFs from Greenland. *Science* 306, 2077–2080. <https://doi.org/10.1126/science.1104639>
- GERMAN, C.R., KLINKHAMMER, G.P., EDMOND, J.M., MITRA, A., ELDERFIELD, H. (1990) Hydrothermal scavenging of rare-earth elements in the ocean. *Nature* 345, 516–518. <https://doi.org/10.1038/345516a0>
- HOLLAND, H.D. (1990) Origins of breathable air. *Nature* 347, 17–17. <https://doi.org/10.1038/347017a0>
- JOHNSON, C., BEARD, B., WEYER, S. (2020) *Iron Geochemistry: An Isotopic Perspective*. Springer Nature Press, Switzerland AG. <https://doi.org/10.1007/978-3-030-33828-2>
- KONHAUSER, K.O., PLANAVSKY, N.J., HARDISTY, D.S., ROBBINS, L.J., WARCHOLA, T.J., HAUGAARD, R., LALONDE, S.V., PARTIN, C.A., OONK, P.B.H., TSIKOS, H., LYONS, T.W., BEKKER, A., JOHNSON, C.M. (2017) Iron formations: A global record of Neoproterozoic to Palaeoproterozoic environmental history. *Earth-Science Reviews* 172, 140–177. <https://doi.org/10.1016/j.earscirev.2017.06.012>
- LYONS, T.W., SEVERMANN, S. (2006) A critical look at iron paleoredox proxies: New insights from modern euxinic marine basins. *Geochimica et Cosmochimica Acta* 70, 5698–5722. <https://doi.org/10.1016/j.gca.2006.08.021>
- LYU, D., DENG, Y., WANG, H., ZHANG, F., REN, R., GAO, Z., ZHOU, C., LUO, Z., WANG, X., BI, L., ZHANG, S., CANFIELD, D.E. (2021) Using cyclostratigraphic evidence to define the unconformity caused by the Mesoproterozoic Qinyu Uplift in the North China Craton. *Journal of Asian Earth Sciences* 206, 104608. <https://doi.org/10.1016/j.jseaeas.2020.104608>
- PLANAVSKY, N.J., REINHARD, C.T., WANG, X.L., THOMSON, D., MCGOLDRICK, P., RAINBIRD, R.H., JOHNSON, T., FISCHER, W.W., LYONS, T.W. (2014) Low Mid-Proterozoic atmospheric oxygen levels and the delayed rise of animals. *Science* 346, 635–638. <https://doi.org/10.1126/science.1258410>
- POULTON, S.W., CANFIELD, D.E. (2005) Development of a sequential extraction procedure for iron: implications for iron partitioning in continentally derived particulates. *Chemical Geology* 214, 209–221. <https://doi.org/10.1016/j.chemgeo.2004.09.003>
- RAISWELL, R., CANFIELD, D.E. (2012) The Iron Biogeochemical Cycle Past and Present. *Geochemical Perspectives* 1, 1–220. <https://doi.org/10.7185/geochempersp.1.1>
- RUDNICK, R.L., GAO, S. (2003) Composition of the continental crust. In: HOLLAND, H.D., TUREKIAN, K.K. (Eds.) *Treatise on Geochemistry*. Elsevier–Pergamon, Oxford, UK, 1–64. <https://doi.org/10.1016/B0-08-043751-6/03016-4>
- SALTZMAN, M.R., THOMAS, E. (2012) Carbon Isotope Stratigraphy. In: GRADSTEIN, F.M., OGG, J.G., OGG, M.S.G. (Eds.) *The Geologic Time Scale*. Elsevier, Amsterdam, The Netherlands, 207–232. <https://doi.org/10.1016/B978-0-444-59425-9.00011-1>
- TANG, D., SHI, X., JIANG, G., WU, T., MA, J., ZHOU, X. (2018) Stratiform siderites from the Mesoproterozoic Xiamaling Formation in North China: Genesis and environmental implications. *Gondwana Research* 58, 1–15. <https://doi.org/10.1016/j.gr.2018.01.013>
- YANG, X., ZHANG, Z., SANTOSH, M., DUAN, S., LIANG, T. (2018) Anoxic to suboxic Mesoproterozoic ocean: Evidence from iron isotope and geochemistry of siderite in the Banded Iron Formations from North Qilian, NW China. *Precambrian Research* 307, 115–124. <https://doi.org/10.1016/j.precamres.2018.01.007>
- ZHANG, S., WANG, X., WANG, H., BJERRUM, C.J., HAMMARLUND, E.U., COSTA, M.M., CONNELLY, J.N., ZHANG, B., SU, J., CANFIELD, D.E. (2016) Sufficient oxygen for animal respiration 1,400 million years ago. *Proceedings of the National Academy of Sciences* 113, 1731–1736. <https://doi.org/10.1073/pnas.1523449113>
- ZHANG, S., WANG, H., WANG, X., YE, Y. (2021) The Mesoproterozoic Oxygenation Event. *Science China: Earth Science* 64, 2043–2068. <https://doi.org/10.1007/s11430-020-9825-x>



Isotope evidence for the coupled iron and carbon cycles 1.4 billion years ago

H.J. Wang, Y.T. Ye, Y. Deng, X.M. Wang, E.U. Hammarlund, H.F. Fan,
D.E. Canfield, S.C. Zhang

Supplementary Information

The Supplementary Information includes:

- Geological Background
- Methods
- Table S-1
- Figures S-1 to S-4
- Supplementary Information References

Geological Background

The North China Craton

The North China Craton (NCC) is an old craton with a maximum age of well-preserved gneiss of ~3.8 Ga and an area of $\sim 3 \times 10^6$ km². After the formation of a continental nucleus (>3.3 Ga) and the growth of a massive continental crust (2.9–2.7 Ga) (Jia *et al.*, 2019), the western and eastern blocks of the NCC separately completed micro-block assembly and cratonisation at *ca.* 2.5 Ga. The western and eastern blocks amalgamated along the Trans-North China Orogen (TNCO) to constitute a unified basement at *ca.* 1.85 Ga, eventually forming the present tectonic framework of the NCC (Fig. S-1). The continental growth, assembly and breakup of the NCC from 2.5–1.3 Ga is considered an essential component of the assembly of the Columbia supercontinent (Li *et al.*, 2020).

According to the global paleogeographic reconstruction model for the process of the assembly and breakup of the Columbia supercontinent (Pisarevsky *et al.*, 2014), the NCC was considered to be adjacent to Australia during 1.77–1.41 Ga (Zhang *et al.*, 2017). In addition, putative stratigraphic correlations also provide new evidence that the NCC, Siberia and North Australia might have been neighbours and formed a single large intracratonic basin in the Columbia supercontinent (Mitchell *et al.*, 2021).

The Yanliao Basin

From 1.85–1.80 Ga, the tectonic properties of the NCC shifted from compressional to extensional, and remained so for almost one billion years (1.80–0.80 Ga) or perhaps longer (Zhao and Zhai, 2013). Several rift systems (basins) were

formed successively along the margins of the NCC, including the Xiong'er Basin at the southern margin, the Helan-Jinshan Basin at the southwestern margin, and the Zha'ertai-Bayan Obo-Huade and Yanliao basins at the northern margin (Fig. S-1). The Yanliao Basin is a typical intracratonic rift basin that extends from the northeastern end to the interior of the NCC. Geometrically, it can be divided into two branches: one oriented in a nearly northeast-east direction in the north and the other oriented in a nearly north-south direction in the south (Lu *et al.*, 2002; Deng *et al.*, 2021). However, the basin structure might have undergone a major change at *ca.* 1.6 Ga, connecting with the open sea in the north direction (Zhang *et al.*, 2021). The Xiamaling Formation (1.42–1.35Ga) was likely deposited in an offshore basin (Zhang *et al.*, 2019; Lyu *et al.*, 2021).

In the Yanliao Basin, the Paleo- and Mesoproterozoic sediments are found with a maximum thickness of up to 8000 m (Meng *et al.*, 2011). From bottom to top, these sediments can be classified as the clastic rock-dominated Changchengian System (including the Changzhougou, Chuanlinggou, Tuanshanzi, and Dahongyu formations), the carbonate rock-dominated Jixian System (including the Gaoyuzhuang, Yangzhuang, Wumishan, Hongshuizhuang, and Tieling formations), and the clastic-rock-dominated Xiamaling Formation (Fig. S-2). The duration and boundary ages of the Changchengian and Jixian systems, and the Xiamaling Formation have been well defined by using the U-Pb ages of zircons or baddeleyites from the ash layers, volcanic rocks and intrusive rocks (Fig. S-2).

The structural evolution and sedimentary sequences of the Yanliao Basin during 1.8–1.3 Ga are believed to be related to the breakup of the Columbia supercontinent (Deng *et al.*, 2021; Zhang *et al.*, 2021). Therefore, hydrothermal vents should have been active in a vicinity for an extended period of time. Evidence for hydrothermal contributions to basin geochemistry include the iron formation of the Chuanlinggou Formation (*ca.* 1640Ma) (Lin *et al.*, 2019), the manganese deposit and polymetallic pyrite deposit of the Gaoyuzhuang Formation (*ca.* 1590 Ma) (Gao *et al.*, 2021; Jin *et al.*, 2022), the syndepositional chert bands and nodules of the Wumishan Formation (*ca.* 1490 Ma) (Shen *et al.*, 2018), the black shale events of the Hongshuizhuang Formation (*ca.* 1460 Ma) (Ma *et al.*, 2017), and the iron formation of the Xiamaling Formation (Canfield *et al.*, 2018; Tang *et al.*, 2018). However, there is no direct evidence for the position of hydrothermal vents during the deposition of the Xiamaling iron formation.

The Xiamaling Formation

The Xiamaling Formation is mainly composed of shale and siltstone, and deposited over the carbonate rocks of the Tieling Formation with a parallel unconformity. Two zircon U-Pb TIMS ages (1384.4 ± 1.4 Ma and 1392.0 ± 1.0 Ma; Zhang *et al.*, 2015) and a zircon U-Pb LA-ICP-MS age (1418 ± 14 Ma; Lyu *et al.*, 2021) have been obtained from the volcanic ash layers in the middle and bottom of the Xiamaling Formation, respectively (Fig. S-3). In addition, abundant baddeleyite U-Pb ages of *ca.* 1320 Ma, obtained from the intruded gabbro-diorite sills (Li *et al.*, 2009; Liu *et al.*, 2011; Zhang *et al.*, 2017; Wang *et al.*, 2020), are considered to be accompanied by pre-magmatic uplift that started at about 1350 Ma (Zhang *et al.*, 2017), further constraining that the minimum age of the Xiamaling Formation should be older than 1350 Ma (Fig. S-2). Independent studies gave geological and paleogeographic evidence of an open system of the Yanliao Basin during the whole of the Xiamaling depositional period (Zhang *et al.*, 2019; Gao *et al.*, 2021; Wang *et al.*, 2020; Lyu *et al.*, 2021; Mitchell *et al.*, 2021).

Based on lithological characteristics, the Xiamaling Formation has been traditionally divided into four stratigraphic members in ascending order (*e.g.*, Tang *et al.*, 2018; Fig. S-3). Comparing the outcrop and core from the Xiahuayuan section (N 40°28'13.41", E 115°15'52.9"), we have made a detailed geochemical and sedimentological investigation of the Xiamaling Formation (*e.g.*, Zhang *et al.*, 2015; Wang *et al.*, 2017; Canfield *et al.*, 2018; Zhang *et al.*, 2019), and have suggested a stratigraphic division scheme of 6 lithologic units (Fig. S-3). More detailed petrological and mineralogical descriptions of the Xiamaling iron formation can be seen in Canfield *et al.* (2018) and Tang *et al.* (2018).



Methods

Sample collection

All samples for geochemical analysis were obtained from a fresh drill core, where drilling was conducted with fresh water as the drilling fluid to minimise contamination. Fresh core samples were collected and crushed to powders with a diameter of $<75 \mu\text{m}$ by using a tungsten carbide grinding disc.

Elemental measurements

Major and trace elements were determined at the Analytical Laboratory of Beijing Research Institute of Uranium Geology, China National Nuclear Corporation, after the methods described in [Zhang *et al.* \(2015\)](#). Briefly, major elements were determined using a Philips PW2400 X-ray fluorescence spectrometer (XRF). The relative standard deviations (RSD) of Fe and Al were both lower than 1.0 %. Trace elements were obtained on an ELEMENT XR inductively coupled plasma mass spectrometer (ICP-MS) after rock powders were subjected to complete digestion following the procedures described in [Zhang *et al.* \(2015\)](#). The resulting RSD of each rare earth element concentration was $<1.5 \%$. Accuracies were also tested with the shale standard (GBW 03014) that was measured along with the samples. The concentrations of the interest elements were within 10 % of their reported values.

TOC measurement

Samples for TOC measurement were de-carbonated and combusted in a LECO CS-230HC carbon/sulphur analyser at the Key Laboratory of Petroleum Geochemistry, China National Petroleum Corporation and following the procedures described in [Canfield *et al.* \(2018\)](#). The resulting RSD of each sample was lower than 2.0 %.

Diagenetic minerals measurement

Diagenetic minerals of samples were determined through X-ray diffraction (XRD) analysis with a Rigaku MiniFlex X-ray diffractometer using a 600 W Cu- α source. The measurement were performed at the Key Laboratory of Petroleum Geochemistry, China National Petroleum Corporation and following procedures described in [Canfield *et al.* \(2018\)](#). The data were acquired through measurements of 10° per min over a range from 10° to 70° and analysed in the PDXL Software.

Carbon isotope measurement

Carbon isotopes of carbonate ($\delta^{13}\text{C}_{\text{carb}}$) and organic carbon ($\delta^{13}\text{C}_{\text{org}}$) of the samples were measured at the Key Laboratory of Petroleum Geochemistry, China National Petroleum Corporation and the University of Southern Denmark, after the methods described in [Canfield *et al.* \(2018\)](#). Briefly, pure kerogen was extracted from rocks through HCl and HF treatment as fully described in [Zhang *et al.* \(2016\)](#). The $\delta^{13}\text{C}_{\text{org}}$ values were measured on the extracted kerogens by using a Flush EA 1112 HT O/H-N/C combined with a Delta V Advantage mass spectrometer. The $\delta^{13}\text{C}_{\text{carb}}$ of each sample was determined by reacting with phosphoric acid in an online carbonate preparation device and analysis on a Finnigan Mat-252 mass spectrometer (Thermo Scientific). All $\delta^{13}\text{C}$ values were reported relative to the Vienna Pee Dee Belemnite (VPDB), with standard deviation (SD) of each sample was lower than 0.2 ‰ based on replicate analysis.

Extractable Fe^{2+} and Fe^{3+} analysis

We found that the standard iron speciation protocol ([Poulton and Canfield, 2005](#)) did not effectively extract the siderite in our samples due to their high contents. This was apparent as residues identifiable as siderite by XRD analysis were present after the “Fe carbonate” phase of the standard protocol. For this reason, we applied an HCl acid digestion procedure to these samples. This procedure involved reacting the samples overnight at 50°C with 0.5 M HCl. This procedure was effective at removing both siderite and iron oxides from the sample. After extraction, samples were reacted with ferrozine to determine the Fe^{2+} contents.



Separate splits of each sample were also reacted with hydroxylamine to reduce Fe^{3+} to Fe^{2+} . This solution was reacted with ferrozine to yield total extractable iron, and the difference between the total extractable iron and the iron extracted as Fe^{2+} yielded the Fe^{3+} contents. This procedure was effective at removing iron from siderite and iron oxide-rich samples in the IF, but it might have also removed some silicate-bound iron in the clastic-rich samples. Analyses were conducted at the University of Southern Denmark. Details of the protocol used in partitioning between Fe^{2+} and Fe^{3+} can be found in [Viollier *et al.* \(2000\)](#).

Chromium reduction method

Pyrite sulphur was extracted by Cr reduction, trapped as Ag_2S , with concentrations calculated gravimetrically ([Canfield *et al.*, 1986](#)). Replicate extractions of PACS-2 and in-house standards indicated an analytical uncertainty of <5 %. These extractions were conducted at the University of Southern Denmark.

Iron isotope compositions analysis

The iron isotope compositions were measured at the Laboratory of Isotope Geology, Institute of Geology, Chinese Academy of Geological Sciences. The protocols used are briefly summarised here.

For iron isotope analyses, whole rock powders were digested with $\text{HF}+\text{HNO}_3+\text{HCl}+\text{HClO}_4$. After complete dissolution, the final solution was treated with concentrated HCl repeatedly to convert the cations to a chloride-form. The solution after HCl treatment was finally dissolved in 6 M HCl plus 0.001 % H_2O_2 for chemical purification of Fe^{3+} . The AG MP-1 anion exchange resin was used in the chromatographic separation procedure of Fe^{3+} . Samples were loaded and first washed with 6 M HCl plus 0.001% H_2O_2 to remove ions other than Fe^{3+} and Zn^{2+} , then 2 M HCl plus 0.001% H_2O_2 was used to strip Fe^{3+} from Zn^{2+} . Iron isotope ratios were determined in high mass resolution mode on a Nu Plasma high resolution multi-collector inductively coupled plasma mass spectrometer (HR MC-ICP-MS) using standard-sample bracketing (SSB) approach. Samples were introduced into the mass spectrometer in 0.1 M HNO_3 using a DSN 100 desolating nebulizer with 5 ppm Fe^{3+} . The $^{56}\text{Fe}/^{54}\text{Fe}$ ratio of each sample was reformulated into $\delta^{56}\text{Fe}$ -notation and expressed in units of per mille (‰), relative to the reference material of IRMM-014 as follows:

$$\delta^{56}\text{Fe} (\text{‰}) = \left[\frac{(^{56}\text{Fe}/^{54}\text{Fe})_{\text{sample}}}{(^{56}\text{Fe}/^{54}\text{Fe})_{\text{standard}}} - 1 \right] \times 1000 \quad (\text{Eq. S-1})$$

The long-term external reproducibility at high-resolution mode is better than 0.05 ‰ at 2 SD. Figure S-4 illustrates the relationship of $\delta^{56}\text{Fe}$ versus $\delta^{57}\text{Fe}$ ratios obtained for all Xiamaling samples. All the data lie on the mass-dependent fractionation line within analytical uncertainty.

Fe cycle and isotope systematics

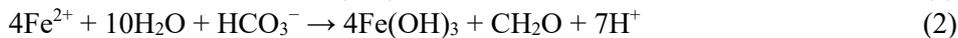
The sources of oceanic Fe^{2+} include hydrothermal fluids, the benthic shuttle from continental margins, and terrestrial input through riverine sources and aerosol deposition. Based on the compilations and models of [Condie \(1993\)](#), the average Fe_T/Al ratios of the Precambrian crust is taken to be 0.46, and average Fe_T/Ti is taken to be 11.23. These compositions would reflect the average detrital input to the ocean, ignoring biogeochemical diagenetic effects. Although riverine and aeolian sources of Fe might be important in the modern and Precambrian oceans, these terrestrial Fe inputs bear no obvious isotopic fractionations ($\Delta^{56}\text{Fe}_{\text{ferrous ion-total iron}}$) and probably had a minimal effect on the Fe isotope compositions ($\delta^{56}\text{Fe}$) of the Mesoproterozoic ferruginous marine waters ([Johnson *et al.*, 2020](#)). For hydrothermal and benthic Fe fluxes, atmospheric O_2 levels and marine sulfate-sulfide would have affected the Fe^{2+} oxidation extents in the oceans, the relative control of sulfides and oxides on isotopic exchange/fractionation with Fe^{2+} , and the Fe mass balances in the oceans. All of which could be recorded in the Fe composition and isotope values of sedimentary rocks.

Based on the modeling of [Kump and Seyfried \(2005\)](#), Precambrian hydrothermal fluids would have had much higher Fe/S ratios, with lower sulfide contents, and much higher Fe^{2+} contents. For the low O_2 and sulfate contents in the Mesoproterozoic ocean, especially in the deep ocean, the Fe^{2+} would have undergone minimal oxidation. Therefore, the $\square^{56}\text{Fe}$ of Fe^{2+} derived from distal hydrothermal plumes should have been preserved in transit to



continental margin basins. In the low-oxygen conditions of the Mesoproterozoic ocean, benthic Fe fluxes controlled by escape of pore fluid Fe²⁺ from marine sediments, might have been a very important source of Fe²⁺ (Raiswell and Canfield, 2012). The benthic Fe flux is also a function of the contents of reactive Fe³⁺, organic carbon (C_{org}), and bottom-water O₂. Sufficient delivery of reactive Fe³⁺ and C_{org} are needed to support dissimilatory iron reduction (DIR) and generate Fe²⁺. Decreased Fe²⁺ oxidation in a low oxygen environment and decreased Fe²⁺ pyritisation in a low sulfide environment will increase the transport of diagenetic Fe²⁺ to water column.

The extremely negative δ¹³C_{carb} values (from -27 ‰ to -8 ‰) of siderites from the XML IFs were suggested to have formed in 3 steps (Canfield *et al.*, 2018), including: 1) oxidation of seawater Fe²⁺ to Fe-oxyhydroxides (Fe(OH)₃), likely at the chemocline of the ancient basin, 2) reduction of the Fe(OH)₃ to diagenetic Fe²⁺ in the water column and sediments, and 3) crystallisation of Fe²⁺ as siderite. The Fe(OH)₃ in step 1 can form either through the oxidation of seawater Fe²⁺ with O₂ (Eq. 1) or from anoxygenic photosynthesis at the chemocline (Eq. 2). Step 1 generates ⁵⁶Fe-enriched Fe-(oxy)hydroxides with an abiotic Δ⁵⁶Fe_{hydroxide-ferrous ion} of *ca.* +3.0 or biotic Δ⁵⁶Fe_{hydroxide-ferrous ion} from +1.5 ‰ to +3.0‰ (Johnson *et al.*, 2020). Step 2 can occur both in the seawater and in the pore-waters, and generates ⁵⁶Fe-depleted diagenetic Fe²⁺ (Eq. 3) with a similar Δ⁵⁶Fe_{ferrous ion-hydroxide} of *ca.* -3.0 ‰ through abiotic or biotic pathways (Johnson *et al.*, 2020). Step 3 occurs in the sediment and generates ⁵⁶Fe-depleted siderite (Eq. 4) with a Δ⁵⁶Fe_{ferrous ion-siderite} of -0.5 ‰ in the abiotic system (Wiesli *et al.*, 2004).



Calculation of the clastic and diagenetic siderite end-members using iron isotope mass balance

Whole rock δ⁵⁶Fe reflect the net Fe isotopic composition of a mixture of different iron-bearing minerals, whose contents and isotopic compositions vary between samples. For the siderite-dominated Xiamaling Iron Formation, the contents of Fe-oxides and pyrite are much lower than siderite. So, clastic Fe and diagenetic siderite were assumed to be the two main endmembers that affect the whole rock δ⁵⁶Fe. A simple mixing model was used to calculate the evolution of δ⁵⁶Fe by mixing between clastic and diagenetic endmembers, whose δ⁵⁶Fe were also refined in the modelling. In our model, the whole rock δ⁵⁶Fe was defined to be:

$$\delta^{56}\text{Fe}_{\text{wh}} = (\text{Fe}_{\text{cla}} \times \delta^{56}\text{Fe}_{\text{cla}} + \text{Fe}_{\text{dia}} \times \delta^{56}\text{Fe}_{\text{dia}}) / (\text{Fe}_{\text{cla}} + \text{Fe}_{\text{dia}}) \quad (\text{Eq. S-2})$$

Here, δ⁵⁶Fe_{wh}, δ⁵⁶Fe_{cla} and δ⁵⁶Fe_{dia} are iron isotopic values of whole rock, clastic endmember and diagenetic endmember, respectively. Fe_{cla} and Fe_{dia} are the iron amounts in the clastic and diagenetic endmembers, respectively. The sum of Fe_{cla} and Fe_{dia} is total Fe (Fe_T).

$$\text{Fe}_T = \text{Fe}_{\text{cla}} + \text{Fe}_{\text{dia}} \quad (\text{Eq. S-3})$$

Fe_{cla} and Fe_{dia} can be further defined as:

$$\text{Fe}_{\text{cla}} = f_{\text{cla-Fe}} \times T_{\text{cla-Fe}} \quad (\text{Eq. S-4})$$

$$\text{Fe}_{\text{dia}} = f_{\text{dia-Fe}} \times T_{\text{dia-Fe}} \quad (\text{Eq. S-5})$$

Here, f_{cla-Fe} and f_{dia-Fe} are the fractions of clastic endmember and diagenetic endmember, respectively. T_{cla-Fe} and T_{dia-Fe} are iron contents of the clastic endmember and diagenetic endmember, respectively. The sum of f_{cla-Fe} and f_{dia-Fe} is 1.



Then, Equation S-2 can be transformed into:

$$\delta^{56}\text{Fe}_{\text{wh}} = T_{\text{cla-Fe}} \times T_{\text{dia-Fe}} \times (\delta^{56}\text{Fe}_{\text{cla}} - \delta^{56}\text{Fe}_{\text{dia}}) / (T_{\text{dia-Fe}} - T_{\text{cla-Fe}}) / \text{Fe}_T + (T_{\text{dia-Fe}} \times \delta^{56}\text{Fe}_{\text{dia}} - T_{\text{cla-Fe}} \times \delta^{56}\text{Fe}_{\text{cla}}) / (T_{\text{dia-Fe}} - T_{\text{cla-Fe}}) \quad (\text{Eq. S-5})$$

So, we can use the formula $Y = a/x + b$ to do the optimal fitting between $\delta^{56}\text{Fe}_{\text{wh}}$ and Fe_T , with

$$a = T_{\text{cla-Fe}} \times T_{\text{dia-Fe}} \times (\delta^{56}\text{Fe}_{\text{cla}} - \delta^{56}\text{Fe}_{\text{dia}}) / (T_{\text{dia-Fe}} - T_{\text{cla-Fe}}) \quad (\text{Eq. S-6})$$

$$b = (T_{\text{dia-Fe}} \times \delta^{56}\text{Fe}_{\text{dia}} - T_{\text{cla-Fe}} \times \delta^{56}\text{Fe}_{\text{cla}}) / (T_{\text{dia-Fe}} - T_{\text{cla-Fe}}) \quad (\text{Eq. S-7})$$

With a $T_{\text{cla-Fe}}$ of 3.6 % (upper crust value; Rudnick and Gao, 2003) and $T_{\text{dia-Fe}}$ of 48 %, the $\delta^{56}\text{Fe}_{\text{cla}}$ and $\delta^{56}\text{Fe}_{\text{dia}}$ can be calculated with the optimised a and b values.

Supplementary Table

Table S-1 Geochemical data of the Xiamaling Iron Formation.

Table S-1 is available for download (Excel file) from the online version of the article at <https://doi.org/10.7185/geochemlet.2208>.



Supplementary Figures

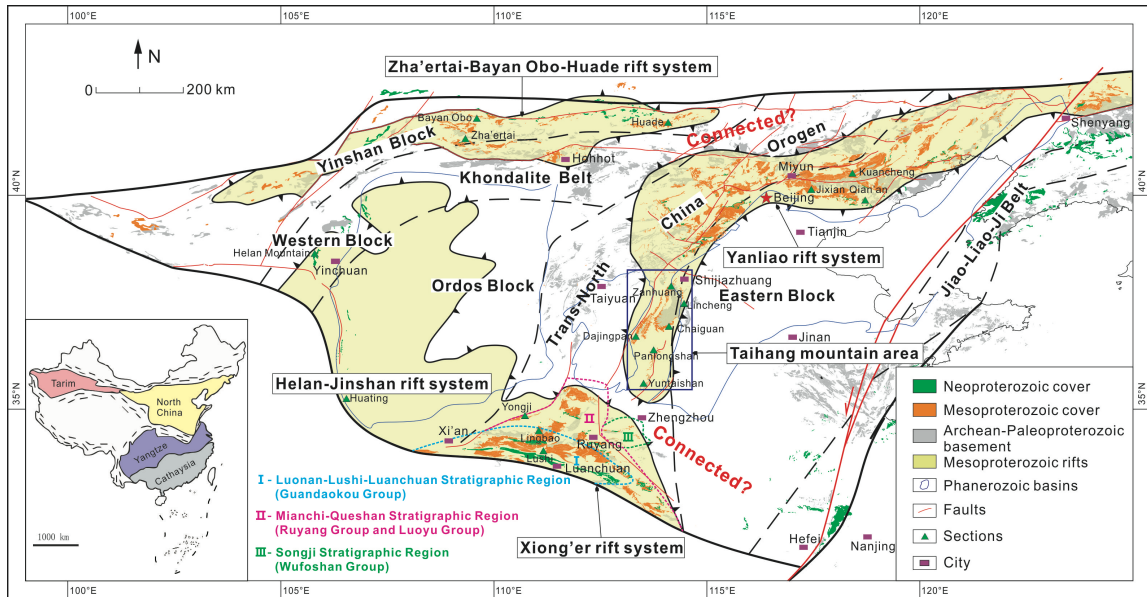


Figure S-1 Distributions of the Proterozoic rift systems (basins) and sedimentary covers in the North China Craton. Modified from Deng *et al.* (2021).

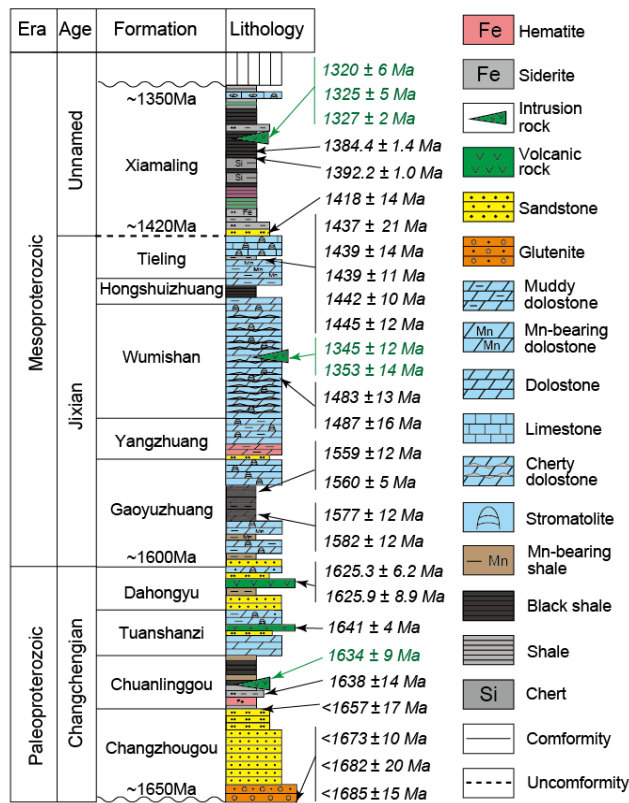


Figure S-2 The Palaeo- and Mesoproterozoic stratigraphic framework and U-Pb ages of zircons or baddeleyites from the ash layers, volcanic rocks and intrusive rocks in the Yanliao Basin, North China Craton. Modified from Zhang *et al.* (2021).



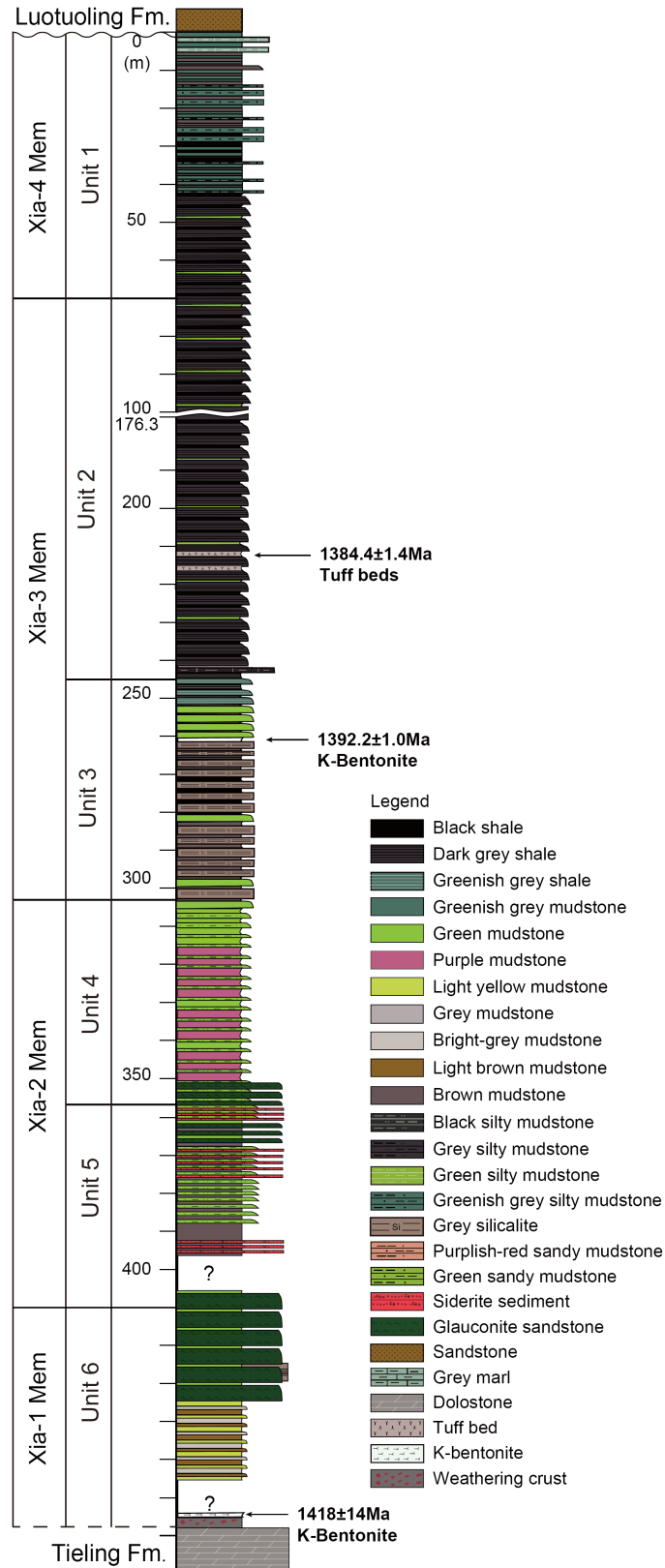


Figure S-3 The stratigraphic column of the Xiamaling Formation in the Yanliao Basin, North China Craton, modified from Zhang *et al.* (2019). The age of 1418 ± 14 Ma is from Lyu *et al.* (2021).



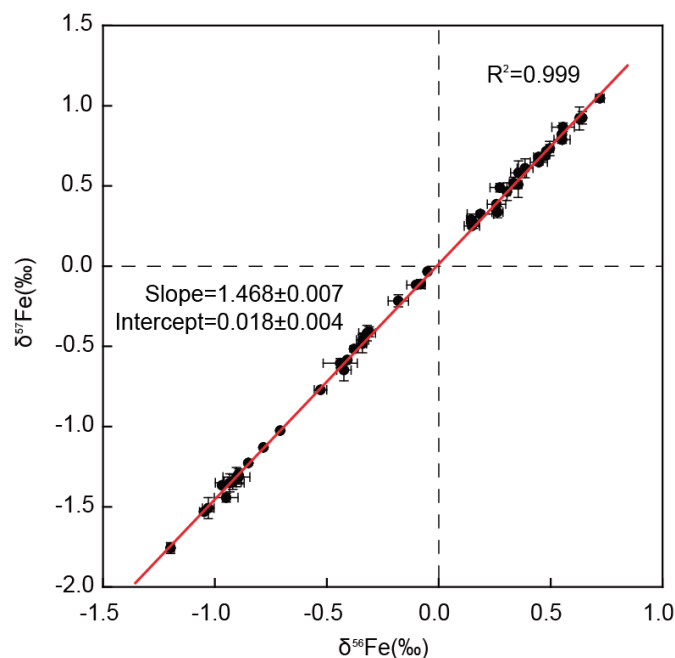


Figure S-4 $\delta^{56}\text{Fe}$ versus $\delta^{57}\text{Fe}$ of the Xiamaling samples normalised by IRMM-014. The red line is the theoretical mass-dependent fractionation line (slope = 1.474) based on a simple harmonic oscillator approximation (Criss, 1999).

Supplementary Information References

- Canfield, D.E., Raiswell, R., Westrich, J.T., Reaves, C.M., Berner, R.A. (1986) The use of chromium reduction in the analysis of reduced inorganic sulfur in sediments and shales. *Chemical Geology* 54, 149–155. [https://doi.org/10.1016/0009-2541\(86\)90078-1](https://doi.org/10.1016/0009-2541(86)90078-1)
- Canfield, D.E., Zhang, S.C., Wang, H.J., Wang, X.M., Zhao, W.Z., Su, J., Bjerrum, C.J., Haxen, E.R., Hammarlund, E.U. (2018) A Mesoproterozoic Iron Formation. *Proceedings of the National Academy of Sciences of the United States of America* 115, E3895–E3904. <https://doi.org/10.1073/pnas.1720529115>
- Condie, K.C. (1993) Chemical composition and evolution of the upper continental crust: contrasting results from surface samples and shales. *Chemical Geology* 104, 1–37. [https://doi.org/10.1016/0009-2541\(93\)90140-E](https://doi.org/10.1016/0009-2541(93)90140-E)
- Criss, R.E. (1999) *Principles of Stable Isotope Distribution*. Oxford University Press, New York. <https://doi.org/10.1093/oso/9780195117752.001.0001>
- Deng Y., Wang H.J., Lyu D., Zhang F.L., Gao, Z.Y., Ren, R., Ye, T.T., Lyu, Y.T., Wang, X.M., Guan, P., Zhang, S.C. (2021) Evolution of the 1.8–1.6 Ga Yanliao and Xiong'er basins, north China Craton. *Precambrian Research* 365, 106383. <https://doi.org/10.1016/j.precamres.2021.106383>
- Gao, B.Y., Zhang, L.C., Jin, X.D., Li, Z.Q., Li, W.J. (2020) Rhenium-Osmium isotope systematics of an Early Mesoproterozoic SEDEX polymetallic pyrite deposit in the North China Craton: Implications for geological significance and the marine osmium isotopic record. *Ore Geology Reviews* 117, 103331. <https://doi.org/10.1016/j.oregeorev.2020.103331>
- Gao, Z.Y., Wang, H.J., Feng, J.R., Luo, Z., Zhang, Y.H., Li, X.H. (2021) Provenance and paleogeographic environment of the Middle Proterozoic Xiamaling formation in Yanliao Basin. *Acta Geologica Sinica* 95, 3606–3628. <http://doi.org/10.19762/j.cnki.dizhixuebao.2020289>. (in Chinese with English abstract)
- Jia, X.L., Zhai, M.G., Xiao, W.J., Sun, Y., Ratheesh-Kumar, R.T., Yang, H., Zhou, K.F., Wu, J.L. (2019) Late Neoproterozoic to early Paleoproterozoic tectonic evolution of the southern North China Craton: Evidence from geochemistry, zircon geochronology and Hf isotopes of felsic gneisses from the Taihua complex.

Precambrian Research 326, 222–239. <https://doi.org/10.1016/j.precamres.2017.11.013>

- Jin, S., Ma, P., Guo, H., Yu, W.C., Xu, L.T., Lin, Q. (2022) Genesis of Mesoproterozoic Gaoyuzhuang Formation manganese ore in Qinjiayu, East Hebei: Constraints from mineralogical and geochemical evidences. *Earth Science*, 47, 277–289. <https://doi.org/10.3799/dqkx.2021.055> (in Chinese with English abstract)
- Johnson, C., Beard, B., Weyer, S. (2020) *Iron Geochemistry: An Isotopic Perspective*. Springer Nature Press, Switzerland AG. <https://doi.org/10.1007/978-3-030-33828-2>
- Kump, L.R., Seyfried, W.E. (2005) Hydrothermal Fe fluxes during the Precambrian: effect of low oceanic sulfate concentrations and low hydrostatic pressure on the composition of black smokers. *Earth and Planetary Science Letters* 235, 654–662. <https://doi.org/10.1016/j.epsl.2005.04.040>
- Li, H.K., Lu, S.N., Li, H.M., Sun, L.X., Xiang, Z.Q., Geng, J.Z., Zhou, H.Y. (2009) Zircon and beddeleyite U-Pb precision dating of basic rock sills intruding Xiamaling Formation, North China. *Geological Bulletin of China* 28, 1396–1404. (in Chinese with English abstract)
- Li, S.Z., Li, X.Y., Wang, G.Z., Liu, Y.M., Wang, Z.C., Wang, T.S., Cao, X.Z., Guo, X.Y., Somerville, I., Li, Y., Zhou, J., Dai, L.M., Jiang, S.H., Zhao, H., Wang, Y., Wang, G., Yu, S. (2020) Global Meso-Neoproterozoic plate reconstruction and formation mechanism for Precambrian basins: constraints from three cratons in China. *Earth-Science Reviews* 198, 102946. <https://doi.org/10.1016/j.earscirev.2019.102946>
- Lin, Y.T., Tang, D.J., Shi, X.Y., Zhou, X.Q., Huang, K.J. (2019) Shallow-marine ironstones formed by microaerophilic iron-oxidizing bacteria in terminal Paleoproterozoic. *Gondwana Research* 76, 1–18. <https://doi.org/10.1016/j.gr.2019.06.004>
- Liu, Y., Zhong, N.N., Tian, Y.J., Qi, W., Mu, G.Y. (2011) The oldest oil accumulation in China: Meso-proterozoic Xiamaling Formation bituminous sandstone reservoirs. *Petroleum Exploration and Development* 38, 503–512. [https://doi.org/10.1016/S1876-3804\(11\)60050-5](https://doi.org/10.1016/S1876-3804(11)60050-5)
- Lu, S.N., Yang, C.L., Li, H.K., Li, H.M. (2002) A group of rifting events in the terminal paleoproterozoic in the North China Craton. *Gondwana Research* 5, 123–131. [https://doi.org/10.1016/S1342-937X\(05\)70896-0](https://doi.org/10.1016/S1342-937X(05)70896-0)
- Lyu, D., Deng, Y., Wang, H.J., Zhang, F.L., Ren, R., Gao, Z.Y., Zhou, C.M., Luo, Z., Wang, X.M., Bi, L.N., Zhang, S.C., Canfield, D.E. (2021) Using cyclostratigraphic evidence to define the unconformity caused by the Mesoproterozoic Qinyu Uplift in the North China Craton. *Journal of Asian Earth Sciences* 206, 104608. <https://doi.org/10.1016/j.jseaes.2020.104608>
- Ma, K., Hu, S.Y., Wang, T.S., Zhang, B.M., Qin, S.F., Shi, S.Y., Wang, K., Huang, Q.Y., (2017) Sedimentary environments and mechanisms of organic matter enrichment in the Mesoproterozoic Hongshuizhuang Formation of northern China. *Palaeogeography, Palaeoclimatology, Palaeoecology* 475, 176–187. <https://doi.org/10.1016/j.palaeo.2017.02.038>
- Meng, Q.R., Wei, H.H., Qu, Y.Q., Ma, S.X. (2011) Stratigraphic and sedimentary records of the rift to drift evolution of the Northern North China Craton at the Paleo- to Mesoproterozoic transition. *Gondwana Research* 20, 205–218. <https://doi.org/10.1016/j.gr.2010.12.010>
- Mitchell, R.N., Kirscher, U., Kunzmann, M., Liu, Y., Cox, G.M. (2021) Gulf of Nuna: Astrochronologic correlation of a Mesoproterozoic oceanic euxinic event. *Geology* 49, 25–29. <https://doi.org/10.1130/G47587.1>
- Pisarevsky, S.A., Elming, S.Å., Pesonen, L.J., Li, Z.X. (2014) Mesoproterozoic paleogeography: supercontinent and beyond. *Precambrian Research* 244, 207–225. <https://doi.org/10.1016/j.precamres.2013.05.014>
- Poulton, S.W., Canfield, D.E. (2005) Development of a sequential extraction procedure for iron: implications for iron partitioning in continentally derived particulates. *Chemical Geology* 214, 209–221. <https://doi.org/10.1016/j.chemgeo.2004.09.003>
- Raiswell, R., Canfield, D.E. (2012) The Iron Biogeochemical Cycle Past and Present. *Geochemical Perspectives* 1, 1–220. <https://doi.org/10.7185/geochempersp.1.1>
- Rudnick, R.L., Gao, S. (2003) Composition of the continental crust. In: Holland, H.D., Turekian, K.K. (Eds.) *Treatise on Geochemistry*. Elsevier-Pergamon, Oxford, 1–64. <https://doi.org/10.1016/B0-08-043751-6/03016-4>



- Shen, B., Ma H.R., Ye, H.Q., Lang, X.G., Pei, H.X., Zhou, C.M., Zhang, S.H., Yang, R.Y. (2018) Hydrothermal origin of syndepositional chert bands and nodules in the Mesoproterozoic Wumishan Formation: Implications for the evolution of Mesoproterozoic cratonic basin, North China. *Precambrian Research* 310, 213–228. <https://doi.org/10.1016/j.precamres.2018.03.007>
- Tang, D.J., Shi, X.Y., Jiang, G.Q., Wu, T., Ma, J.B., Zhou, X.Q. (2018) Stratiform siderites from the Mesoproterozoic Xiamaling Formation in North China: Genesis and environmental implications. *Gondwana Research* 58, 1–15. <https://doi.org/10.1016/j.gr.2018.01.013>
- Viollier, E., Inglett, P.W., Hunter, K., Roychoudhury, A.N., Cappellen, P.V. (2000) The ferrozine method revisited: Fe(II)/Fe(III) determination in natural waters. *Applied Geochemistry* 15, 785–790. [https://doi.org/10.1016/S0883-2927\(99\)00097-9](https://doi.org/10.1016/S0883-2927(99)00097-9)
- Wang, H.Y., Zhang, Z.H., Li, C., Algeo, T.J., Cheng, M., Wang, W. (2020) Spatiotemporal redox heterogeneity and transient marine shelf oxygenation in the Mesoproterozoic ocean. *Geochimica et Cosmochimica Acta* 270, 201–217. <https://doi.org/10.1016/j.gca.2019.11.028>
- Wang, X.M., Zhang, S.C., Wang, H.J., Bjerrum, C.J., Hammarlund, E.U., Haxen, E.R., Su, J., Wang, Y., Canfield, D.E. (2017) Oxygen, climate and the chemical evolution of a 1400 million years old tropical marine setting. *American Journal of Science* 317, 861–900. <https://doi.org/10.2475/08.2017.01>
- Wiesli, R.A., Beard, B.L., Johnson, C.M. (2004) Experimental determination of Fe isotope fractionation between aqueous Fe(II), siderite and “green rust” in abiotic systems. *Chemical Geology* 211, 343–362. <https://doi.org/10.1016/j.chemgeo.2004.07.002>
- Zhang, S.C., Wang, X.M., Hammarlund, E.U., Wang, H.J., Costa, M.M., Bjerrum, C.J., Connelly, J.N., Zhang, B.M., Bian, L.Z., Canfield, D.E. (2015) Orbital forcing of climate 1.4 billion years ago. *Proceedings of the National Academy of Sciences of the United States of America* 112, 1406–1413. <https://doi.org/10.1073/pnas.1502239112>
- Zhang, S.C., Wang, X.M., Wang, H.J., Bjerrum, C.J., Hammarlund, E.U., Costa, M.M., Connelly, J.N., Zhang, B.M., Su, J., Canfield, D.E. (2016) Sufficient oxygen for animal respiration 1,400 million years ago. *Proceedings of the National Academy of Sciences of the United States of America* 113, 1731–1736. <https://doi.org/10.1073/pnas.1523449113>
- Zhang, S.C., Wang, X.M., Wang, H.J., Bjerrum, C.J., Hammarlund, E.U., Haxen, E.R., Wen, H.J., Ye, Y.T., Canfield, D.E. (2019) Paleoenvironmental proxies and what the Xiamaling Formation tells us about the mid-Proterozoic ocean. *Geobiology* 17, 225–246. <https://doi.org/10.1111/gbi.12337>
- Zhang, S.C., Wang, H.J., Wang, X.M., Ye, Y.T. (2021) The Mesoproterozoic Oxygenation Event. *Science China: Earth Science* 64. <https://doi.org/10.1007/s11430-020-9825-x>
- Zhang, S.H., Zhao, Y., Li, X., Ernst, R. E., Yang, Z. (2017) The 1.33–1.30 Ga Yanliao large igneous province in the North China Craton: Implications for reconstruction of the Nuna (Columbia) supercontinent, and specifically with the North Australian Craton. *Earth and Planetary Science Letters* 465, 112–125. <https://doi.org/10.1016/j.epsl.2017.02.034>
- Zhao, G.C., Zhai, M.G. (2013) Lithotectonic elements of precambrian basement in the North China Craton: review and tectonic implications. *Gondwana Research* 23, 1207–1240. <https://doi.org/10.1016/j.gr.2012.08.016>
- Zhu, Y.S., Yang, J.H., Wang, H.; Wu, F.Y. (2020) Mesoproterozoic (~1.32 Ga) modification of lithospheric mantle beneath the North China craton caused by break-up of the Columbia supercontinent. *Precambrian Research* 2020, 342, 105674. <https://doi.org/10.1016/j.precamres.2020.105674>

